Article

Novel Control Technology for Reducing Output Power Harmonics of Standalone Solar Power Generation Systems

Hwa-Dong Liu [1,2,*], Jhen-Ting Lin [2], Xin-Wen Lin [2], Chang-Hua Lin [3] and Shoeb-Azam Farooqui [3,*]

1 Undergraduate Program of Vehicle and Energy Engineering, National Taiwan Normal University, Taipei 106, Taiwan

2 Department of Industrial Education, National Taiwan Normal University, Taipei 106, Taiwan; dylan60411@gmail.com (J.-T.L.); 61170039h@gapps.ntnu.edu.tw (X.-W.L.)

3 Department of Electrical Engineering, National Taiwan University of Science and Technology, Taipei 106, Taiwan; link@mail.ntust.edu.tw

* Correspondence: hdliu@ntnu.edu.tw (H.-D.L.); shoebazam6331@gmail.com (S.-A.F.)

Abstract: This study presents a standalone solar power system that incorporates a photovoltaic (PV) module, a boost converter, an H-bridge inverter, a low-pass filter (LPF), and a microcontroller unit (MCU). A novel cake sweetness maximum power point tracking (CS MPPT) algorithm and adjustable frequency and duty cycle (AFDC) control strategy has been proposed and efficiently applied to the solar power system for optimizing the system efficiency and output power quality. The experimental results show that the proposed CS MPPT algorithm achieves an efficiency of 99% under both the uniform irradiance conditions (UIC) and partial shading conditions (PSC). Subsequently, the AFDC control strategy is applied to the H-bridge inverter which improves the output AC voltage and AC current and thereby improving the power quality. The system ensures a stable 110 V_{rms}/60 Hz AC output voltage with only 2% total voltage harmonic distortion of voltage (THD_v), and produces a high-quality output voltage with reduced LPF volume and better economic benefits. The comparative analysis demonstrates that the characteristics and the performances of the CS MPPT algorithm in combination with the AFDC control strategy is better than the existing several maximum power point tracking (MPPT) techniques and inverter control strategies. The research output affirms the potential of the proposed solar power system to fulfill the actual daily needs of electricity by harnessing the maximum power from PV modules.

Keywords: standalone solar power system; cake sweetness maximum power point tracking; adjustable frequency and duty cycle; total voltage harmonic distortion

1. Introduction

Renewable energy has gained unprecedented attention due to the increasing global concerns about environmental protection, energy conservation, carbon reduction, and achieving net zero emissions. Renewable energy sources including solar power, wind power, hydropower, and tidal power are sustainable alternatives to fossil fuels. Solar power generation is an exceptional renewable energy source owing to its abundance and free availability, noise-free operation, low maintenance cost, prolonged service life of up to 20 years and inherent ability to directly convert sunlight into electrical energy through semiconductor technology [1,2].

Solar power generation systems can be categorized as standalone, grid-connected, and hybrid types. The grid-connected and hybrid systems can be interconnected with the grid, battery banks, diesel generators, and other renewable energy devices [3–5] which allow them to support each other and enhance grid stability. However, their installation costs are relatively high. In contrast, the standalone solar power system market has witnessed a significant growth in recent years [6,7]. Several factors can be attributed to this growth: Firstly, the efforts of governments across the globe to reduce carbon emissions and mitigate

greenhouse effects [8], have led to a strong demand for solar power system development. Secondly, the ongoing research endeavors for improving the efficiency and reliability of standalone power systems, offer longer operation time and lower maintenance costs [9–11]. Thirdly, the standalone solar power systems can provide power to regions without access to the grid or regions with unstable power supply, thus enhancing energy security. Lastly, the commercial standalone systems are now modularized which allows users to assemble and deploy them more conveniently. Therefore, this study focuses on developing control strategies to enhance the performance of standalone solar power generation systems.

Numerous research works have already been performed in the field of solar maximum power point tracking (MPPT) algorithms which play a significant role in optimizing the energy harvest from solar modules [12–18]. Some of the recently proposed algorithms are mentioned here with their advantages. In 2021, Fares et al., proposed the squirrel MPPT algorithm that can quickly track the maximum power point (MPP) in a shaded environment and achieve an efficiency of 99% [12]. In the same year, King et al., presented a hybrid algorithm combining the fireworks algorithm with the particle swarm optimization (PSO), which resulted in a 20% improvement in tracking speed [13]. Zhao et al. (2020) introduced the grain-eating bird (GEB) algorithm combined with a dynamic particle algorithm for MPPT control, enhancing the tracking speed and performance as compared to traditional dynamic particle algorithms [14]. Li et al. (2019) developed a weather-adaptive MPPT technique that substantially surpassed the conventional perturb and observe (P&O) methods, addressing the limitations of power converters and significantly improving efficiency under specific conditions [15]. Furthermore, Mirza et al. (2019) presented a novel rooster swarm algorithm, which demonstrated better performance and speed in MPPT compared to the GEB algorithm and P&O method [16]. Xu et al. (2023) proposed a hybrid quantum particle swarm optimization (HQPSO), which optimizes the particle swarm optimization (PSO), and can effectively capture MPP under PSC. Moreover, the convergence speed of HQPSO surpasses that of the P&O method and PSO [17]. Roh (2022) introduced the deep learning (DL) MPPT algorithm for judging the irradiance level. This algorithm can track changes in irradiance level and adjust the duty cycle to capture MPP. The DL MPPT algorithm demonstrates better performance than the P&O method [18].

The architecture of standalone solar power systems consists of a DC/DC power converter connected to a DC/AC inverter. The primary purpose is to convert the DC power from the solar modules into AC power and produce a single-phase AC 110 V_{rms}/60 Hz for the load. Several studies [19–24] have focused on controlling the DC/AC inverter to ensure excellent power quality, avoid load flickering, and prolong the lifespan of the electrical equipment. Tamer et al. (2009) proposed a new PSO algorithm combined with a multilevel inverter to eliminate voltage harmonics and provide high-quality power [19]. Similarly, Tamer et al. (2008) employed a genetic algorithm combined with a multilevel inverter to reduce complex computations and rapidly decrease voltage harmonics, thus improving power quality [20]. Hamid et al. (2014) presented a three-phase power compensation scheme to reduce voltage harmonics and provide AC sinusoidal voltage at the output [21]. Moreover, Sayari et al. (2016) proposed a self-tuning algorithm for harmonic compensation, ensuring AC sinusoidal output voltage from the inverter [22]. Jiao et al. (2023) proposed a system with multiple H-bridge inverters in series and adjusted their phase angles. This reduced the THD while improving the system output power quality [23]. Muhammad et al. (2023) introduced a hybrid technology for minimizing the THD. This technique includes multi-level inverters and adaptive control, which can effectively reduce power harmonics. However, the control strategy is complex [24].

This study gained inspiration from the contribution made by various scholars on MPPT and power control techniques for solar power systems. The proposed standalone solar power system includes PV modules connected to a boost converter, which is further connected to an H-bridge inverter and a low-pass filter (LPF). The Cake Sweetness (CS) MPPT algorithm has been proposed to achieve MPP in combination with the boost converter. Additionally, an adjustable frequency and duty cycle (AFDC) control strategy is

employed for the inverter to improve power harmonic content and reduce the size of the low-pass filter (LPF). In this study, the proposed novel control strategy helps to enhance the efficiency and economic benefits of the solar power system.

Table 1 presents a comprehensive comparison of eight MPPT algorithms in terms of their characteristics and performance. The proposed CS MPPT algorithm does not require prior knowledge of parameters, has a simple structure, fast convergence time, and exhibits high efficiency under both uniform irradiance conditions (UIC) and partial shade conditions (PSC). Hence, the proposed CS MPPT algorithm outperforms the other seven MPPT algorithms. Table 2 presents a comparison of seven inverter control strategies in terms of their characteristics and performance. The proposed AFDC control strategy does not require prior knowledge of parameters, has a simple structure, and exhibits low power harmonics distortion. Consequently, the proposed AFDC control strategy outperforms the other six control strategies.

Table 1. Comparison of characteristics and performance of several MPPT algorithms.

MPPT Algorithm	Parameter	Complexity	Convergence Time	UIC Performance	PSC Performance
[12]	Necessary	Medium	Medium	High	High
[13]	Necessary	Medium	Medium	High	High
[14]	Necessary	High	Fast	High	High
[15]	Necessary	Medium	Medium	High	Medium
[16]	Necessary	Medium	Medium	High	Medium
[17]	Necessary	Medium	Fast	High	High
[18]	Unnecessary	Medium	Fast	High	Medium
Proposed CS	Unnecessary	Simple	Fast	High	High

Table 2. Comparison of characteristics and performance of several inverter control strategies.

Control Strategy	Parameter	Complexity	Amount of Total Harmonic Distortion
[19]	Unnecessary	Low	Medium
[20]	Unnecessary	Low	Medium
[21]	Necessary	Medium	Medium
[22]	Necessary	Medium	Low
[23]	Unnecessary	Medium	Medium
[24]	Necessary	Complexity	Low
Proposed AFDC	Unnecessary	Low	Low

2. PV Module Specification and Traditional Maximum Power Point Tracking Algorithm

2.1. PV Module Specification

Figure 1 shows the equivalent circuit of a solar cell. The different parameters of this circuit are the output current of the solar cell (I_{pv}), photo-generated current (I_{ph}), reverse saturation current (I_{rs}), solar cell output voltage (V_{pv}), solar cell equivalent series resistance (R_s), solar cell equivalent parallel resistance (R_{sh}), thermal voltage (V_t) and diode ideality factor (A). The relationship between these parameters is mentioned in Equation (1) [25].

$$I_{pv} = I_{ph} - I_{rs}\left[e^{\left(\frac{V_{pv}+R_s I_{pv}}{AV_t}\right)} - 1\right] - \frac{\left(V_t + I_{pv}R_s\right)}{R_{sh}} \tag{1}$$
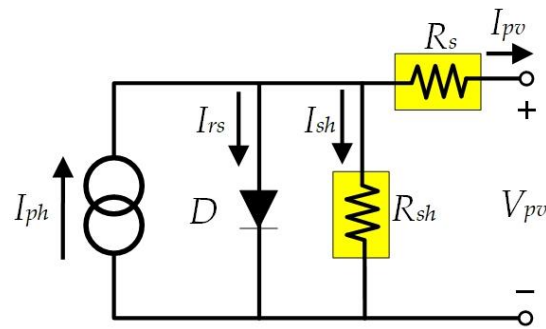
Figure 1. Equivalent circuit of a solar cell.

Equation (2) describes the relationship between thermoelectric voltage (V_t), number of solar cells connected in series (N_s), Boltzmann constant (k), Kelvin temperature (T), and electric charge (q) [25].

$$V_t = \frac{N_s k T}{q} \tag{2}$$

Equation (3) establishes the relationship between the solar cell fill factor (FF), MPP current (I_{MPP}), MPP voltage (V_{MPP}), short-circuit current (I_{sc}), and open-circuit voltage (V_{oc}) [26].

$$FF = (V_{MPP} \cdot I_{MPP})/(V_{oc} \cdot I_{sc}) \tag{3}$$

Equation (4) defines the relationship between solar cell output power (P_{pv}), output voltage (V_{pv}), and output current (I_{pv}).

$$P_{pv} = V_{pv} \cdot I_{pv} \tag{4}$$

Equation (5) depicts the relationship between I_{MPP}, current factor (k_i), and I_{sc}.

$$I_{MPP} = k_i \cdot I_{sc} \tag{5}$$

Equation (6) describes the relationship between V_{MPP}, voltage factor (k_v), and V_{oc}.

$$V_{MPP} = k_v \cdot V_{oc} \tag{6}$$

Multiple solar cells are interconnected in series and parallel configurations to form a PV module. Table 3 shows the specifications of a single PV module used in this study. At a solar irradiance of 1000 W/m^2 and a temperature of 25 °C, the PV module exhibits the following characteristics as displayed in Table 3.

Table 3. Specification of a single PV module.

Parameter	Value
Open-circuit Voltage (V_{oc})	36.5 V
Short-circuit Current (I_{sc})	9.5 A
Maximum power point voltage (V_{MPP})	28.5 V
Maximum power point current (I_{MPP})	8.5 A
Maximum power point power (P_{MPP})	242 W

2.2. Traditional Maximum Power Point Tracking Algorithm

Solar power generation systems are susceptible to changes in the environment, which can affect their output power. Therefore, it is essential to employ an MPPT algorithm to capture the MPP and ensure high efficiency in solar power generation systems. Traditional MPPT algorithms include the open-circuit voltage method, short-circuit current method, hill-climbing (HC) algorithm, P&O method, and three-point weight method [27–31]. The advantages of these methods are their simplicity, ease of implementation, and cost-effectiveness. However,

their disadvantages include the inability to capture the MPP under shading conditions and their perturbative characteristics, which can impact system efficiency. To address the shortcomings of the traditional MPPT algorithms, the Cake Sweetness (CS) MPPT algorithm has been introduced in this study. The CS MPPT algorithm is capable of capturing the MPP under both the UIC and PSC, thus improving its perturbative characteristics as well as enhancing the system efficiency.

3. Proposed System

3.1. Stand-Alone Solar Power System Architecture

The architecture diagram of the proposed control strategy applied to a standalone solar power system has been illustrated in Figure 2. Firstly, the system architecture consists of a PV module connected to a boost converter, followed by an H-bridge inverter and an LPF. Secondly, the boost converter incorporates the CS MPPT algorithm, enabling the solar power system to capture the MPP during operation. Finally, the H-bridge inverter integrates the AFDC control strategy and allows the system to provide a 110 V_{rms}/60 Hz output power supply with a low harmonic distortion amount.
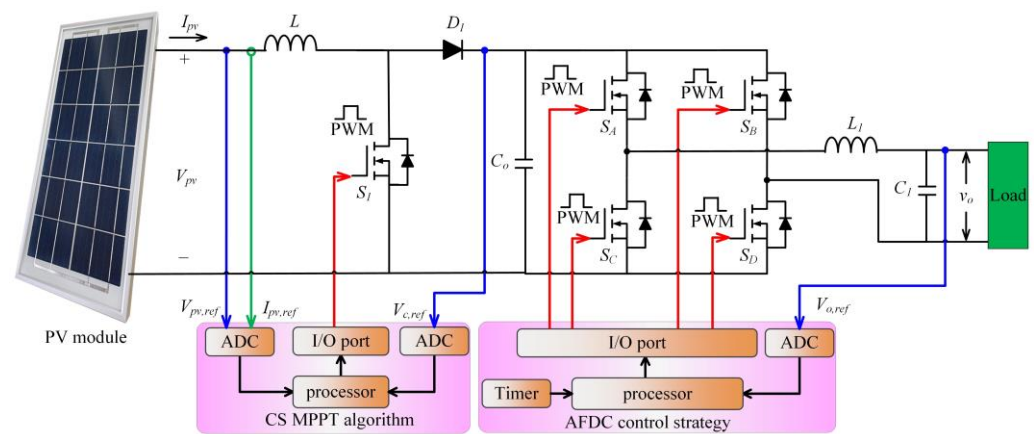

Figure 2. Architecture diagram of the proposed control strategy applied to a standalone solar power system.

The relationship between the variable V_{pv}, output voltage (V_c), and duty cycle (D) of the boost converter in continuous conduction mode (CCM) are represented as follows [25].

$$\frac{V_c}{V_{pv}} = \frac{1}{1-D} \tag{7}$$

Equation (8) gives the relationship between the I_{pv}, output current (I_c), and D in the boost converter CCM [25].

$$I_c = I_{pv}(1-D) \tag{8}$$

The equation relating the inductor value of boost converter (L), minimum input voltage ($V_{pv,min}$), D, switching frequency (f_s), and peak-to-peak inductor current (ΔI) are given as follows [32].

$$L = \frac{\sqrt{2} \cdot V_{pv,\min} \cdot D}{f_s \cdot \Delta I} \tag{9}$$

Equation (10) describes the relationship between the system output AC voltage [$v_o(t)$], output peak voltage (v_{pk}), and phase difference (φ) [32].

$$v_o\left(t\right) = v_{pk}\sin(wt + \varphi) \tag{10}$$

The equation defining the relationship between the root mean square voltage of system output (v_{rms}), $v_o(t)$, and period (T) is provided as follows [32].

$$v_{rms} = \sqrt{\frac{1}{T}\int_0^T [v_o(t)]^2 dt} \tag{11}$$

The equation for the LPF resonant frequency (f_o), inductor value (L_1), and capacitor value (C_1) are expressed as follows [32].

$$f_o = \frac{1}{2\pi\sqrt{L_1 \cdot C_1}} \tag{12}$$

Equation (13) depicts the relationship between the total voltage harmonic distortion (THD$_v$), fundamental frequency voltage [$v^{(1)}$], and each order of voltage harmonic [32].

$$\text{THD}_v = \frac{\sqrt{\sum_{i=2}^{\infty}\left[v^{(i)}\right]^2}}{v^{(1)}} \tag{13}$$

The equation for the total current harmonic distortion (THD$_i$), fundamental frequency current [$i^{(1)}$], and each order of current harmonic amount are provided as follows [32].

$$\text{THD}_i = \frac{\sqrt{\sum_{i=2}^{\infty}\left[i^{(i)}\right]^2}}{i^{(1)}} \tag{14}$$

3.2. Novel Maximum Power Point Tracking Technique

The P_{pv}–V_{pv} characteristics of the PV module under different atmospheric conditions are demonstrated in Figure 3. Figure 3a shows the P_{pv}–V_{pv} characteristic of the PV module under the UIC which exhibits a single MPP. Figure 3b displays the P_{pv}–V_{pv} characteristic of the PV module under the PSC, which exhibits a single MPP but two peak power points (PPP) PPP$_1$ and PPP$_2$.
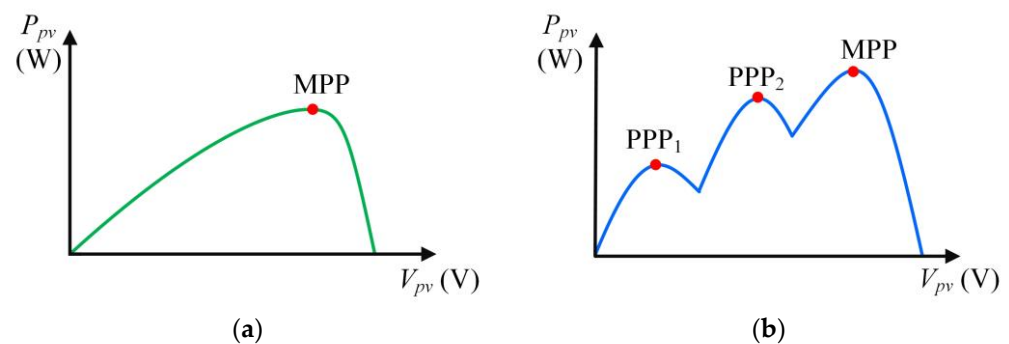

Figure 3. The P_{pv}–V_{pv} characteristic of the PV module: (**a**) under uniform irradiance conditions, (**b**) under partial shade conditions.

To overcome the limitations of traditional MPPT algorithms [25–29] in capturing the MPP under both the UIC and PSC, a novel CS MPPT algorithm has been developed. Inspired by a cake-shaped design, the PV module is divided into six proportional slices as depicted in Figure 4. The sweetness level of each slice is analyzed to determine the proximity to the MPP, with higher sweetness indicating a higher P_{pv}. Through an iterative approach, the CS MPPT algorithm narrows down the MPPT range and ultimately captures the MPP. This method is applicable to both UIC and PSC.
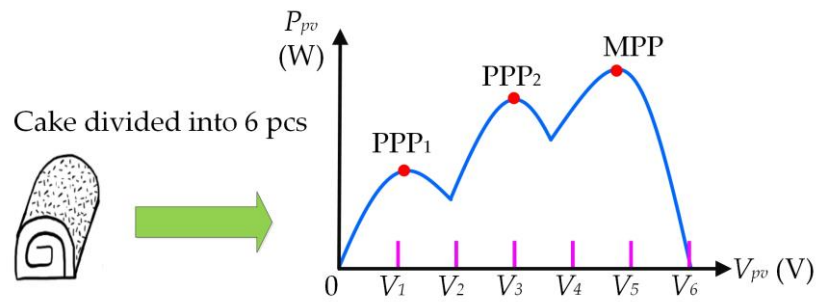
Figure 4. Schematic diagram of the proposed CS MPPT algorithm.

The proposed CS MPPT algorithm is combined with a boost converter for MPPT (as shown in Figure 2). After the CS MPPT algorithm performs its calculations, it outputs the duty cycle to drive the boost converter to capture the MPP. The relationship between P_{pv} and the duty cycle in the proposed CS MPPT algorithm is depicted in Figure 5, which corresponds to the slices shown in Figure 4. Using this P_{pv}–V_{pv} characteristic, the curve is divided into six segments: 0–V_1, V_1–V_2, V_2–V_3, V_3–V_4, V_4–V_5, and V_5–V_6, each of which corresponds to a binary linear equation. Equation (15) is used to calculate the P_{pv} for each segment. The sweet point corresponding to the MPP can be estimated with these calculations.

$$P_{pv} = x \cdot (V_{pv})^2 + y \cdot V_{pv} + z \tag{15}$$
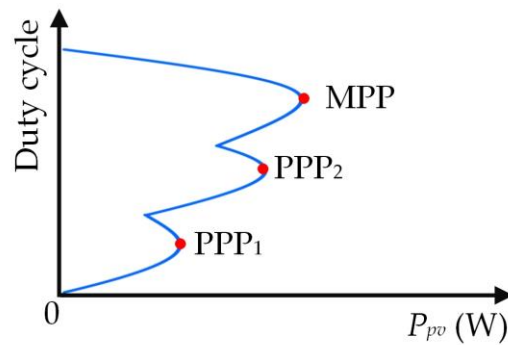

Figure 5. Relationship diagram of P_{pv} and the duty cycle in the proposed CS MPPT algorithm.

The parameters x, y, and z are the coefficients in the above equation.

The proposed CS MPPT algorithm will generate four distinct states by dividing the P_{pv}–V_{pv} curve into six segments. Each state is determined using Equation (15), resulting in three power points for each state (as shown in Figure 6). State 1 represents the region of the curve with the peak power point, while State 3 represents the region with local low points. State 2 and State 4 represent regions that have not yet reached the MPP and the PPP, respectively.

Four distinct states of the P_{pv}–V_{pv} curve of the PV module are demonstrated in Figure 6. Firstly, the proposed CS MPPT algorithm will exclude State 2, State 3, and State 4 to enhance the efficiency of MPPT execution. Next, the P_{pv}–V_{pv} curve exhibits three peak power points. Further comparison is conducted to identify two possible peak power points, denoted as PPP_1 and PPP_2, along with the actual MPP (as shown in Figure 6). Finally, the proposed CS MPPT algorithm can quickly search for the MPP under both UIC and PSC. This significantly improves the efficiency of the solar power generation system and effectively mitigates the shading issues that the PV module may encounter, which could otherwise lead to decreased system efficiency.
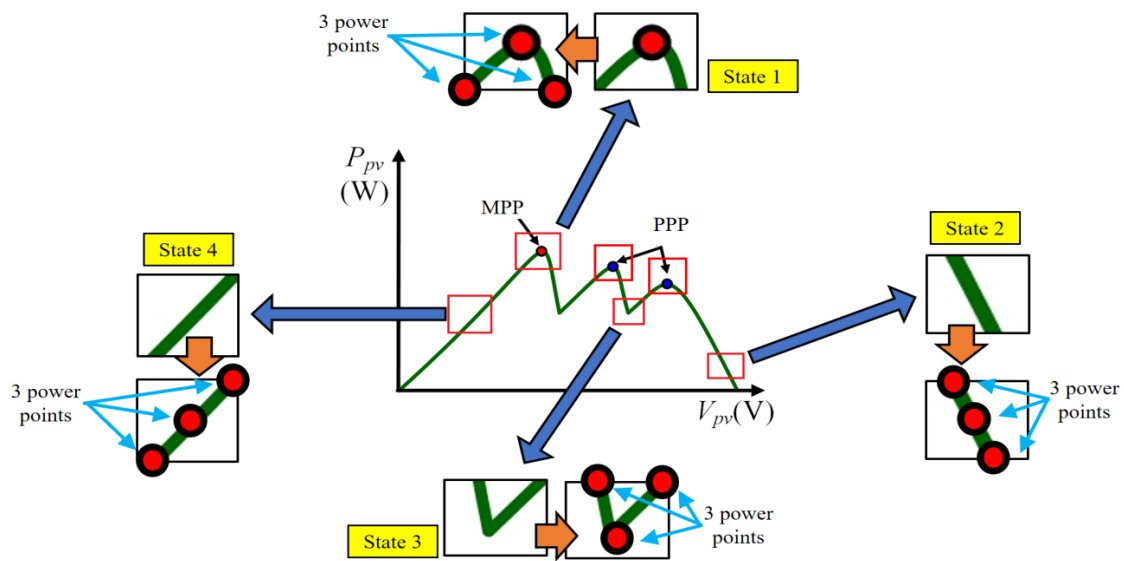
Figure 6. Four different states of P_{pv}–V_{pv} curve of PV module.

3.3. Novel Control Strategy for H-Bridge Inverter

In this article, the adjustable frequency and duty cycle (AFDC) control strategy has been adopted for the H-bridge inverter in the standalone solar power generation system. This control strategy enables the solar energy system to produce a stable 110 V_{rms} AC voltage at a frequency of 60 Hz while maintaining high power quality. Additionally, the AFDC control strategy facilitates a reduction in the LPF size and leads to improved system performance and economic benefits. The AFDC control strategy operates as follows.

Figure 7 displays a representation of the adjustable frequency control strategy. Figure 7a illustrates the relationship between the sinusoidal control signal V_s, triangular wave V_{tri}, and duty cycle. The duty cycle is obtained by comparing V_s with V_{tri}, and this research controls V_{tri} to adjust the frequency of the duty cycle. Figure 7b shows the mechanism of the adjustable frequency control with the relationship between v_o, V_s, and time. Here, v_o is 110 V_{rms}, and t_1 is 16.66 ms (i.e., frequency is 60 Hz). The control of V_{tri} is divided into five intervals, namely T_1 to T_5. The duration of each interval is as follows: T_1 interval is from 0 to 2 ms, T_2 interval is from 2 ms to 6.33 ms, T_3 interval is from 6.33 ms to 10.33 ms, T_4 interval is from 10.33 ms to 14.66 ms, and T_5 interval is from 14.66 ms to 16.66 ms. The V_{tri} frequency is set to 5 kHz for T_1, T_3, and T_5 intervals, while it is set to 1 kHz for T_2 and T_4 intervals, constituting the adjustable frequency control strategy in this research.
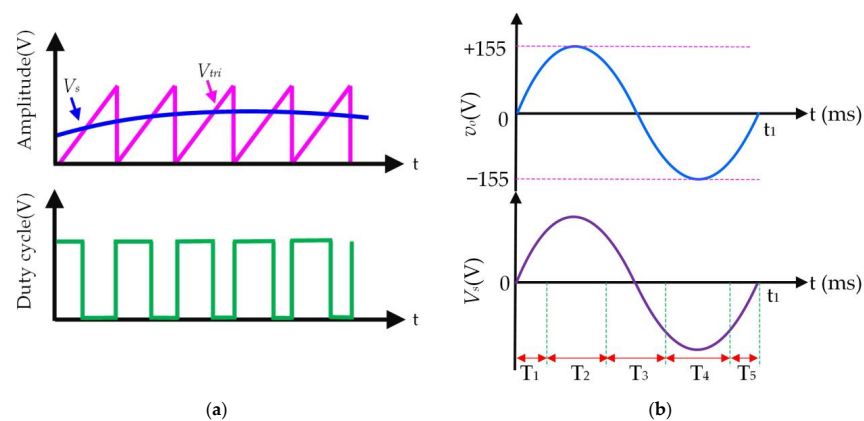

Figure 7. Diagram of adjustable frequency control strategy: (**a**) Illustration of the relationship between sinusoidal control signal V_s, triangular wave V_{tri}, and duty cycle, (**b**) Illustration of the adjustable frequency control mechanism with the Illustration of the relationship of v_o, V_s, and time.

Figure 8 displays the diagram of adjustable duty cycle control strategy and depicts the relationship between v_o, duty cycle, and time. V_o is 110 V_{rms} and t_1 is 16.66 ms (i.e., frequency is 60 Hz). The duty cycle range is set from 0.05 to 0.95. The parameters a, b, and c are utilized to modulate the duty cycle D through time to control the H-bridge inverter. The relationship between D and parameters a, b, and c with the system output voltage [$v_o(t)$] are expressed in Equation (16).

$$D = a \cdot [v_o(t)]^2 + b \cdot [v_o(t)] + c \tag{16}$$

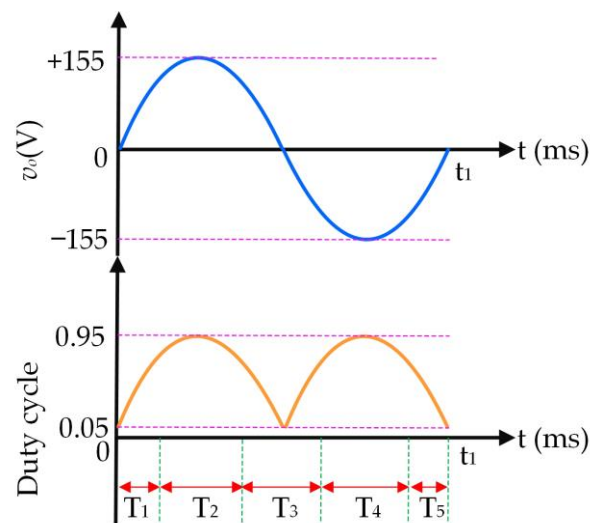where, $a = 1 \times 10^{-5}$, $b = 0.005$, and $c = -0.07$.

Figure 8. Diagram of adjustable duty cycle control strategy with relationship of v_o, duty cycle, and time.

The proposed AFDC control strategy involves variable frequency and modulated duty cycle to effectively control the four Power MOSFETs in the H-bridge inverter, reducing power harmonics distortion and achieving a high-quality output power of 110 V_{rms}/60 Hz. Additionally, this control strategy operates at the frequency of 1 kHz and 5 kHz, thereby improving the conventional operation at 60 Hz, thus addressing the issue of bulky LPF. This improvement results in reduced LPF size and enhanced economic benefits.

The flowchart for the proposed control strategy is depicted in Figure 9. Initially, the output current of PV module must be between 0 and 9.5 A (as Table 3). This means that the system has a connected load that can provide power. In cases where the current is greater than 9.5 A and exceeds the design capacity, the system must be stopped. The output voltage of PV module is then checked which should be greater than 15 V. If it meets the condition, the boost converter is activated to control the voltage output at 155 V_{DC}. Subsequently, the AFDC control strategy is initiated, enabling the H-bridge inverter to operate and resulting in a system output power of 110 V_{rms}/60 Hz. If the boost converter output voltage cannot achieve the desired 155 V_{DC}, the proposed CS MPPT algorithm is activated which allows the boost converter to adjust its output voltage in the range of 140 V_{DC} to 155 V_{DC}. Upon entering the desired range, the AFDC control strategy is triggered, and the H-bridge inverter starts to operate and provides the system output power of 110 V_{rms}/60 Hz. In cases where the boost converter's output voltage cannot be adjusted within the range of 140 V_{DC} to 155 V_{DC} despite using the proposed CS MPPT algorithm, the system will stop operating. Finally, this study combines the standalone solar power generation system with novel control techniques, namely, the proposed CS MPPT algorithm and the AFDC control strategy. This novel control technique offers advantages such as reduced LPF size, enhanced system performance, improved power quality, and economic benefits.
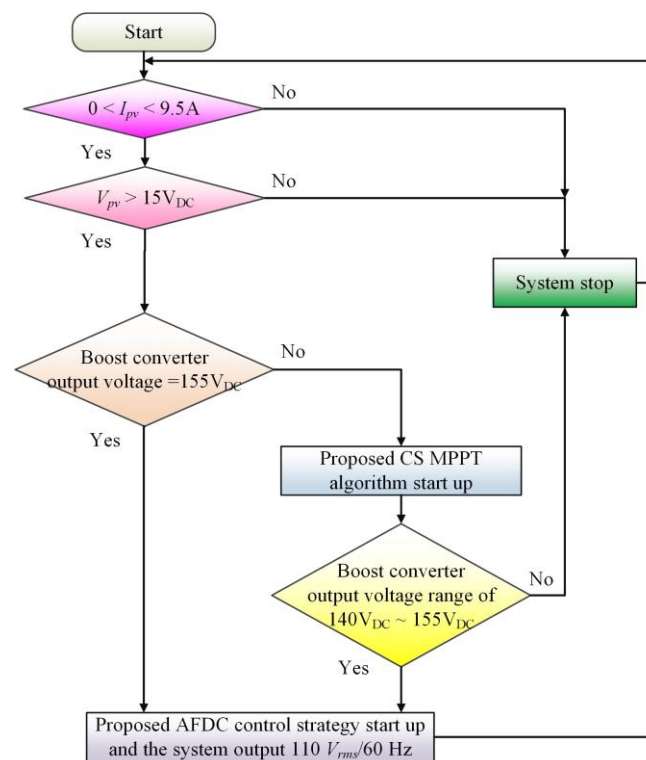
Figure 9. Flowchart for the proposed control strategy.

4. Hardware Implementation and Experimental Results

4.1. Implementation of the Proposed Novel Control Strategy to Standalone Solar Power Generation System

The proposed novel control strategy has been applied to the stand-alone solar power generation system and is physically illustrated in Figure 10. Initially, the standalone solar power generation system is constructed using a PV simulator (as detailed in Table 3) which is supervised by a computer. Subsequently, the PV simulator output terminal is connected to the boost converter, which is embedded in controller 1 (MCU 1). The MCU 1 receives the PV simulator output voltage signal ($V_{pv,ref}$) and the current signal ($I_{pv,ref}$), and the output voltage signal ($V_{c,ref}$) of boost converter. A voltage regulation control is further performed through the proposed control strategy (as Figure 9). Thereby, the boost converter controls the output voltage to 155 V_{DC}. However, if the boost converter output voltage cannot reach 155 V_{DC}, the proposed CS MPPT algorithm (as Equation (15) and Figure 6) will be implemented to allow the boost converter to control the output voltage within the range of 140 V_{DC}–155 V_{DC}. Secondly, the boost converter output terminal is connected to the H-bridge inverter, which is embedded in controller 2 (MCU 2). The MCU 2 receives the output voltage signal $V_{o,ref}$ from the stand-alone solar power generation system and further implements the AFDC control strategy (as Equation (16) and Figures 7 and 8). The execution of the AFDC control strategy allows the H-bridge inverter produce an output voltage with lower THD. Finally, an LPF is connected at the output terminal of the H-bridge inverter to achieve a high-quality AC output of 110 V_{rms}/60 Hz.

Table 4 shows the specifications of the equipment/components used during the hardware implementation of the proposed novel control strategy for the stand-alone solar power generation system. The proposed solar power generation system has been validated as shown in Figures 11–14. These experimental results demonstrate that the proposed solar power generation system has high efficiency and excellent power quality.
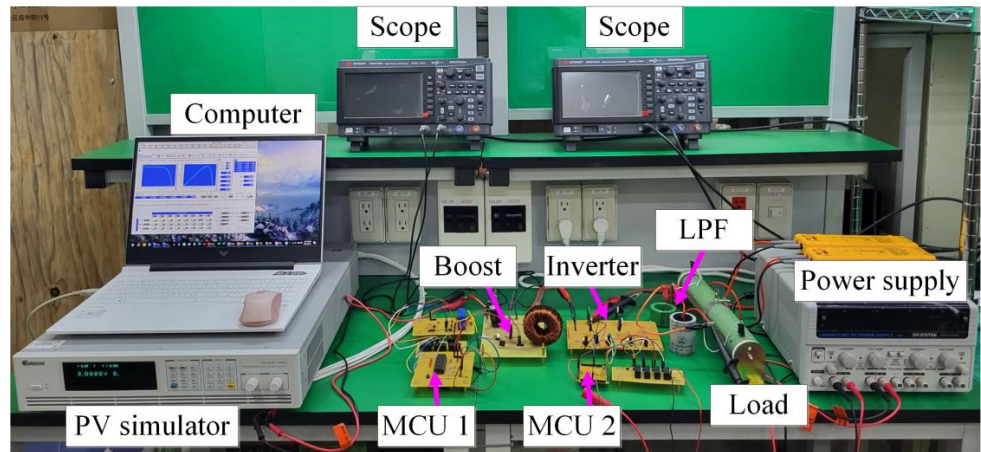
Figure 10. Hardware implementation of the proposed novel control strategy to the standalone solar power generation system.

Table 4. Specifications of the equipment used in hardware implementation of proposed control strategy.

| Equipment/Components		Specification
PV simulator		Chroma, 62020H
Scope		Keysight, DSOX1204A
Power supply		Gwinstek, GPS−4303
Load		130 Ω and 200 Ω
Computer		HP, Victus
Microcontroller unit 1 (MCU 1)		Microchip, 18F452
Microcontroller unit 2 (MCU 2)		Microchip, dsPIC33FJ64GS606
Boost converter		Input voltage:15 V_{DC}−40 V_{DC}, output voltage: 155 V_{DC}
H-bridge inverter		Input voltage: 155 V_{DC}, output voltage: 110 V_{rms}/60 Hz
Low-pass filter (LPF)	Inductance value	100 µH
	Capacitance value	400 V_{AC}, 20 µF

(a)

(b)
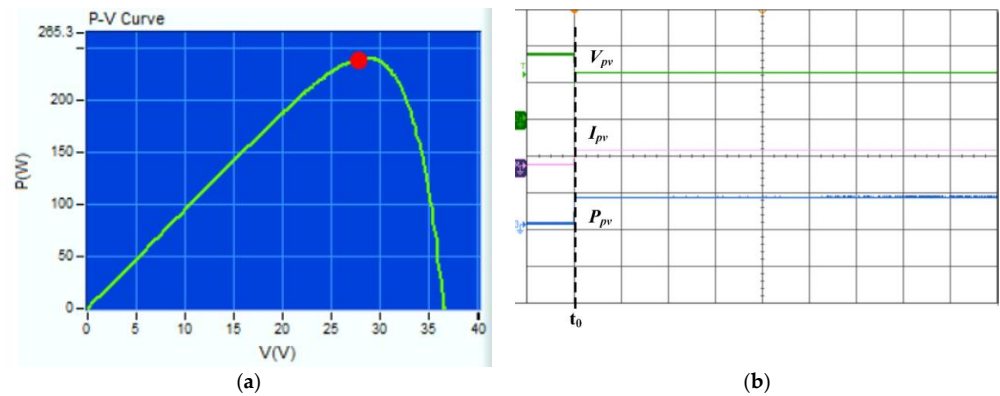
Figure 11. Waveforms of the experimental result of the proposed CS MPPT algorithm under the UIC with solar irradiance of 1000 W/m^2 and temperature of 25 °C: (**a**) actual output P_{pv}–V_{pv} curve from the PV simulator, (**b**) waveforms of V_{pv}, I_{pv}, and P_{pv} from the PV simulator (V_{pv}: 20 V/div, I_{pv}: 20 A/div, P_{pv}: 300 W/div, horizontal axis: 2 s/div).
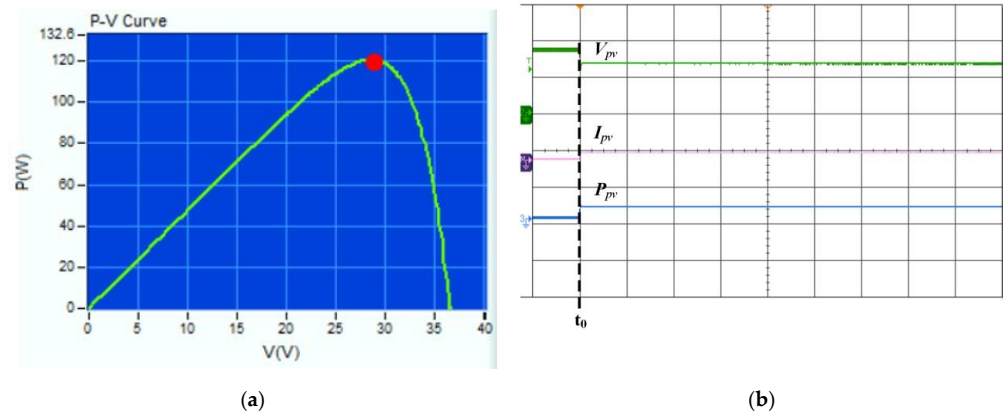
(a)

(b)

Figure 12. Waveforms of the experimental result of the proposed CS MPPT algorithm under the UIC with solar irradiance of 500 W/m^2 and temperature of 25 °C: (**a**) actual output P_{pv}–V_{pv} curve from the PV simulator, (**b**) waveforms of V_{pv}, I_{pv}, and P_{pv} from the PV simulator (V_{pv}: 20 V/div, I_{pv}: 20 A/div, P_{pv}: 300 W/div, horizontal axis: 2 s/div).

Figure 13. PV module under shading condition at solar irradiance of 1000 W/m^2 and temperature of 25 °C.

(a)

(b)

Figure 14. Waveforms of the experimental result of the proposed CS MPPT algorithm under the PSC with solar irradiance of 1000 W/m^2 and temperature of 25 °C: (**a**) actual output P_{pv}–V_{pv} curve from the PV simulator, (**b**) waveforms of V_{pv}, I_{pv}, and P_{pv} from the PV simulator (V_{pv}: 20 V/div, I_{pv}: 20 A/div, P_{pv}: 300 W/div, horizontal axis: 2 s/div).
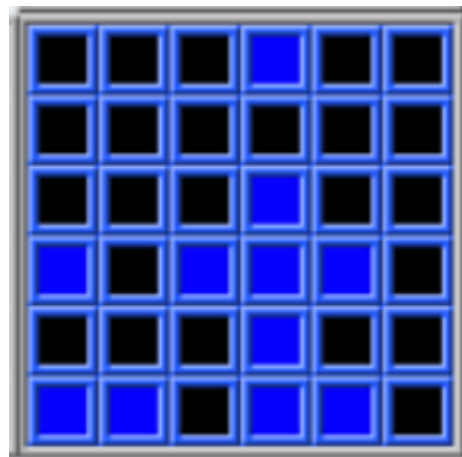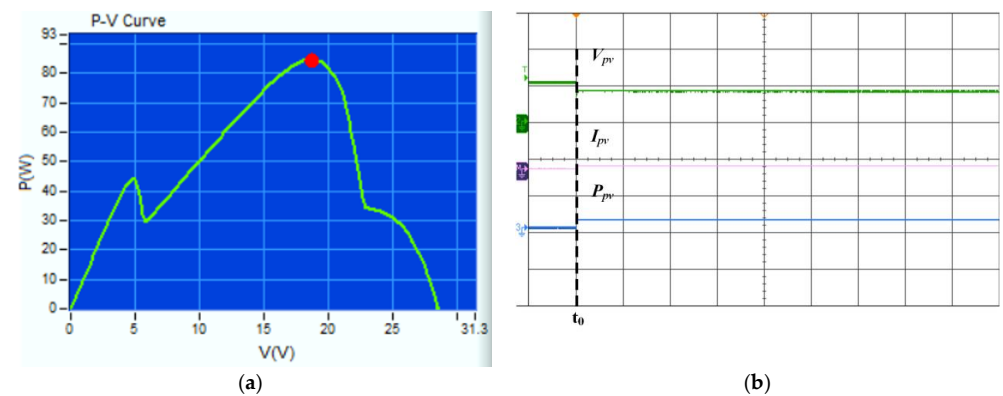
4.2. Experimental Results of the Proposed CS MPPT Algorithm

The waveforms of the experimental result of the proposed CS MPPT algorithm under UIC with a solar irradiance of 1000 W/m^2 and temperature of 25 °C are presented in Figure 11. Figure 11a shows the actual output P_{pv}–V_{pv} curve from the PV simulator and exhibits the MPP at 242 W. Figure 11b displays the waveforms of V_{pv}, I_{pv}, and P_{pv} from the PV simulator. At time t$_0$, the proposed CS MPPT algorithm is activated and quickly operates at the MPP. At this moment, V_{pv} is 28.5 V, I_{pv} is 8.45 A, and P_{pv} is 241 W (as depicted in Figure 11a), and yields an MPP efficiency of 99%.

The waveforms of the experimental result of the proposed CS MPPT algorithm in the UIC with a lower solar irradiance of 500 W/m^2 and temperature of 25 °C are demonstrated in Figure 12. Figure 12a illustrates the actual output P_{pv}–V_{pv} curve from the PV simulator, and exhibits the MPP at 120 W. Figure 12b shows the waveforms of V_{pv}, I_{pv}, and P_{pv} from the PV simulator. At time t$_0$, the proposed CS MPPT algorithm is activated and quickly operates at the MPP. At this moment, V_{pv} is 28 V, I_{pv} is 4.25 A, and P_{pv} is 119 W (as depicted in Figure 12a) and yields an MPP efficiency of 99%.

The schematic diagram of a PV module experiencing a shading condition, with solar irradiance of 1000 W/m^2 and temperature of 25 °C are illustrated in Figure 13. The diagram is simulated using a PV simulator, having a total of 36 solar cells, out of which 25 cells are shaded. In this scenario, the MPP of the PV module is 81.5 W, with V_{MPP} of 18.5 V and I_{MPP} of 4.4 A. Figure 14 presents the waveforms of the experimental result of the proposed CS MPPT algorithm in a PSC with solar irradiance of 1000 W/m^2 and temperature of 25 °C. Figures 13 and 14 provide the complementary information. Figure 14a shows the actual output P_{pv}–V_{pv} characteristic from the PV simulator, which exhibits two peak power points and one MPP and exhibits the MPP at 81.5 W. Figure 14b displays the waveforms of V_{pv}, I_{pv}, and P_{pv} from the PV simulator. At time t$_0$, the proposed CS MPPT algorithm is activated and rapidly operates at the MPP, resulting in V_{pv} of 18 V, I_{pv} of 4.5 A, and P_{pv} of 81 W (as indicated in Figure 14a) and yielding an MPP efficiency of 99%.

It is obvious from Figures 11, 12 and 14 that the proposed CS MPPT algorithm can quickly capture the MPP under both the UIC and PSC and achieve a system efficiency of 99%. The performance of the proposed MPPT algorithm under PSC is better than the algorithms used in ref. [15,16] (as shown in Table 5).

Table 5. Comparison of efficiency between three MPPT algorithms under PSC.

Algorithm	Efficiency
[15]	97%
[16]	94%
Proposed CS MPPT algorithm	99%

4.3. Experimental Results of the Proposed AFDC Control Strategy

Figure 15 shows the measured waveforms of the output voltage (v_o) and current (i_o) of the standalone solar power generation system. In Figure 15a, the system is connected to a load of 130 Ω, resulting in v_o of 110 V$_{rms}$/60 Hz, i_o of 0.85 A$_{rms}$/60 Hz and voltage total harmonic distortion (THD$_v$) of 2%. In Figure 15b, the system is connected to a load of 200 Ω, resulting in v_o of 110 V$_{rms}$/60 Hz, i_o of 0.55 A$_{rms}$/60 Hz and THD$_v$ of 2%.

The implementation of the AFDC control strategy in the standalone solar power generation system ensures the stable operation of v_o at 110 V$_{rms}$/60 Hz with a THDv of 2%. The proposed AFDC control strategy is applied to the standalone solar power generation system, allowing v_o to stably operate at 110 V$_{rms}$/60 Hz with a THD$_v$ of 2%. This control strategy not only ensures excellent power quality but also facilitates the LPF size reduction and thereby reduces the overall system design cost.
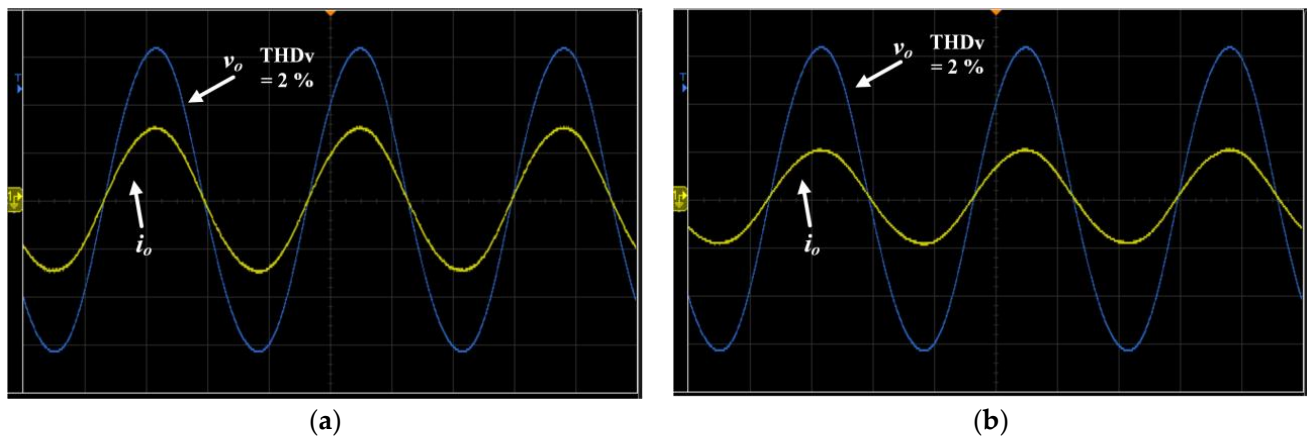
(**a**)

(**b**)

Figure 15. Output voltage (v_o) and current (i_o) waveforms of the standalone solar power generation system at different load: (**a**) load of 130 Ω, (**b**) load of 200 Ω. (v_o: 50 V/div, i_o: 0.75 A/div, horizontal axis: 5 ms/div).

From Figure 15, it is obvious that the proposed AFDC control strategy exhibits excellent power quality with a THD_v of 2%. The THD_v of the proposed system is better than the control methods used in the ref. [19,21] (as shown in Table 6).

Table 6. Comparison of the THD_V of three control strategies.

Control Strategy	THD_v
[19]	5.4%
[21]	9.7%
Proposed AFDC control strategy	2%

5. Discussion and Conclusions

This research introduced a novel control strategy designed for standalone solar power generation systems, aiming to enhance the system efficiency and reduce the THD of the system output voltage. By improving the power quality, reducing the system size, and promoting cost-effectiveness, the proposed approach contributes to the advancement of solar power technology. The developed CS MPPT algorithm and AFDC control strategy were successfully implemented into the standalone solar power generation system and validated through experimental tests. The system achieved 99% MPPT efficiency under both UIC and PSC. The AC output voltage was controlled at 110 V_{rms}/60 Hz and THD_v of 2%, ensuring stable and high-quality power supply. Furthermore, the AFDC control strategy's operation at the frequencies of 1 kHz and 5 kHz effectively addresses the issue of bulky LPF associated with traditional 60 Hz frequency operation. Therefore, the system's cost-effectiveness is optimized by reducing the LPF size. The performance of the proposed method was evaluated and then compared with seven existing MPPT techniques and six inverter control strategies. The results clearly demonstrate that the proposed method outperformed comparative approaches in terms of efficiency and characteristics. The solar power generation system in this research efficiently converts solar energy into electricity and thus can be used to meet real-world electricity demands effectively.

In this study, the proposed novel control strategy when combined with a stand-alone solar power generation system, exhibits excellent performance which has been validated through experimental results. The proposed CS MPPT algorithm can capture MPP under both the UIC and PSC with a single PV module. It can analyze the P_{pv}–V_{pv} characteristic curve of the PV module in a wide range, and then capture MPP. Therefore, this technique can also be applied to PV arrays. In addition, an H-bridge inverter combined with an AFDC control strategy are used in the system which can generate high-quality output power. However, if this AFDC control strategy is used in a three-phase inverter, additional phase

shift control must be added to facilitate the use of different inverters. As the proposed novel control strategy design has been used for conventional solar power generation system hardware, the control strategy can suitably be expanded to larger stand-alone solar power generation systems. It can even be used in grid-connected and hybrid solar power generation systems.

In the future, the proposed control strategy can be applied to other renewable energy systems and integrated with the grid and energy storage systems. Further extensions could involve combining it with high-gain power converters to alleviate the burden of voltage boost, thereby enhancing the performance of various renewable energy systems.

Author Contributions: Conceptualization, H.-D.L., J.-T.L. and X.-W.L.; formal analysis, H.-D.L., J.-T.L. and X.-W.L.; investigation, H.-D.L., J.-T.L. and X.-W.L.; software, H.-D.L., J.-T.L. and X.-W.L.; methodology, H.-D.L., J.-T.L. and X.-W.L.; data curation, H.-D.L., J.-T.L. and X.-W.L.; visualization H.-D.L., J.-T.L. and X.-W.L.; funding acquisition, H.-D.L.; supervision, H.-D.L.; writing—original draft, H.-D.L., J.-T.L., X.-W.L., C.-H.L. and S.-A.F.; writing–review & editing, H.-D.L., J.-T.L., X.-W.L., C.-H.L. and S.-A.F. All authors have read and agreed to the published version of the manuscript.

Data Availability Statement: Not applicable.

Conflicts of Interest: The authors declare no conflict of interest.

Nomenclature

I_{pv}	Output current of the solar cell	S_A, S_B, S_C, S_D	H-bridge inverter's power MOSFET
I_{ph}	Photo-generated current	L_1	Inductor of low-pass filter
I_{rs}	Reverse saturation current	C_1	Capacitor of low-pass filter
V_{pv}	Solar cell output voltage	f_s	Switching frequency
R_s	Solar cell equivalent series resistance	$\triangle I$	Peak-to-peak inductor current
R_{sh}	Solar cell equivalent parallel resistance	$v_o(t)$	The system output AC voltage
V_t	Thermal voltage	φ	Phase difference
A	Diode ideality factor	v_{rms}	Root mean square voltage of system output
V_t	Thermoelectric voltage	f_o	Resonant frequency
N_s	Number of solar cells connected in series	$v^{(1)}$	Fundamental frequency voltage
k	Boltzmann constant	$i^{(1)}$	Fundamental frequency current
T	Kelvin temperature	x	Parameter x of Equation (15)
q	Electric charge	y	Parameter y of Equation (15)
k_i	Current factor	z	Parameter z of Equation (15)
k_v	Voltage factor	a	Parameter a of Equation (16)
S_1	Boost converter's power MOSFET	b	Parameter b of Equation (16)
L	Boost converter's inductor	c	Parameter c of Equation (16)
D_1	Boost converter's diode	V_s	Sinusoidal control signal
C_o	Boost converter's capacitor	V_{tri}	Triangular wave

References

1. Alves, E.F.; Polleux, L.; Guerassimoff, G.; Korpås, M.; Tedeschi, E. Allocation of Spinning Reserves in Autonomous Grids Considering Frequency Stability Constraints and Short-Term Solar Power Variations. *IEEE Access* **2023**, *11*, 29896–29908. [CrossRef]
2. Khan, R.A.; Liu, H.-D.; Lin, C.-H.; Lu, S.-D.; Yang, S.-J.; Sarwar, A. A Novel High-Voltage Gain Step-Up DC–DC Converter with Maximum Power Point Tracker for Solar Photovoltaic Systems. *Processes* **2023**, *11*, 1087. [CrossRef]
3. Alikhani, A.M.; Mahmoudi, A.; Khezri, R.; Kahourzade, S. Multiobjective Optimization of System Configuration and Component Capacity in an AC Minigrid Hybrid Power System. *IEEE Trans. Ind. Appl.* **2022**, *58*, 4158–4170. [CrossRef]
4. Debnath, S.; Marthi, P.R.V.; Xia, Q.; Pan, J.; Saeedifard, M.; Vipin, V.N.; Chakraborty, S.; Arifujjaman, M. Renewable Integration in Hybrid AC/DC Systems Using a Multi-Port Autonomous Reconfigurable Solar Power Plant (MARS). *IEEE Trans. Power Syst.* **2021**, *36*, 603–612. [CrossRef]

5. Sami, B.S. Intelligent Energy Management for Off-Grid Renewable Hybrid System Using Multi-Agent Approach. *IEEE Access* **2020**, *8*, 8681–8696. [CrossRef]

6. Hasabelrasul, H.; Cai, Z.; Sun, L.; Suo, X.; Matraji, I. Two-Stage Converter Standalone PV-Battery System Based on VSG Control. *IEEE Access* **2022**, *10*, 39825–39832. [CrossRef]

7. Guillén-Asensio, A.; Sanz-Gorrachategui, I.; Bono-Nuez, A.; Bernal, C.; Alcaine, J.M.S.; Cebolla, F.J.P. Energy Shortage Failure Prediction in Photovoltaic Standalone Installations by Using Machine Learning Techniques. *IEEE Access* **2021**, *9*, 158660–158671. [CrossRef]

8. 27th Climate Change Conference of Parties (COP 27) Data. Available online: https://www.bbc.com/zhongwen/trad/world-63 698710 (accessed on 21 November 2022).

9. Sabir, B.; Lu, S.-D.; Liu, H.-D.; Lin, C.-H.; Sarwar, A.; Huang, L.-Y. A Novel Isolated Intelligent Adjustable Buck-Boost Converter with Hill Climbing MPPT Algorithm for Solar Power Systems. *Processes* **2023**, *11*, 1010. [CrossRef]

10. Liu, H.-D.; Farooqui, S.-A.; Lu, S.-D.; Lee, Y.-L.; Lin, C.-H. A Novel SLOPDM Solar Maximum Power Point Tracking Control Strategy for the Solar Photovoltaic Power System. *Processes* **2022**, *10*, 1452. [CrossRef]

11. Lu, S.-D.; Lin, C.-H.; Huang, L.-Y.; Lee, Y.-L.; Liu, H.-D.; Liao, P.-C.; Gao, G.-J.; Hsu, C.-M. Novel Global-MPPT Control Strategy Considering the Variation in the Photovoltaic Module Output Power and Loads for Solar Power Systems. *Processes* **2022**, *10*, 367. [CrossRef]

12. Fares, D.; Fathi, M.; Shams, I.; Mekhilef, S. A novel global MPPT technique based on squirrel search algorithm for PV module under partial shading conditions. *Energy Convers. Manag.* **2021**, *230*, 113773–113784. [CrossRef]

13. King, L.G.; Gopal, C.L.; Juwono, F.H.; Chiong, C.W.R.; Ling, H.-C.; Basuki, T.A. A novel global MPPT technique using improved PS-FW algorithm for PV system under partial shading conditions. *Energy Convers. Manag.* **2021**, *246*, 114639–114655.

14. Zhao, Z.; Cheng, R.; Yan, B.; Zhang, J.; Zhang, Z.; Zhang, M.; Lai, L.L. A dynamic particles MPPT method for photovoltaic systems under partial shading conditions. *Energy Convers. Manag.* **2020**, *220*, 113070–113084. [CrossRef]

15. Li, S. A variable-weather-parameter MPPT control strategy based on MPPT constraint conditions of PV system with inverter. *Energy Convers. Manag.* **2019**, *197*, 111873–111886. [CrossRef]

16. Mirza, A.F.; Mansoor, M.; Ling, Q.; Yin, B.; Javed, M.Y. A Salp-Swarm Optimization based MPPT technique for harvesting maximum energy from PV systems under partial shading conditions. *Energy Convers. Manag.* **2019**, *209*, 112625–112650. [CrossRef]

17. Xu, X.; Zhou, W.; Xu, W.; Nie, Y.; Chen, S.; Ou, Y.; Zhou, K.; Liu, M. Application of the MPPT Control Algorithm Based on Hybrid Quantum Particle Swarm Optimization in a Photovoltaic Power Generation System. *Processes* **2023**, *11*, 1456. [CrossRef]

18. Roh, C. Deep-Learning Algorithmic-Based Improved Maximum Power Point-Tracking Algorithms Using Irradiance Forecast. *Processes* **2022**, *10*, 2201. [CrossRef]

19. Tamer, K.A.-O.; Abdelhamid, H. Elimination of harmonics in multilevel inverters with non-equal dc sources using PSO. *Energy Convers. Manag.* **2009**, *50*, 756–764. [CrossRef]

20. Tamer, K.E.-N.; Abdelhamid, H. Selective harmonic elimination of new family of multilevel inverters using genetic algorithms. *Energy Convers. Manag.* **2008**, *49*, 89–95. [CrossRef]

21. Hamid, M.I.; Jusoh, A. Reduction of waveform distortion in grid-injection current from single-phase utility interactive PV-inverter. *Energy Convers. Manag.* **2014**, *85*, 212–226. [CrossRef]

22. Sayari, N.A.; Chilipi, R.; Barara, M. An adaptive control algorithm for grid-interfacing inverters in renewable energy based distributed generation systems. *Energy Convers. Manag.* **2016**, *111*, 443–452. [CrossRef]

23. Jiao, N.; Wang, S.; Ma, J.; Liu, T.; Zhou, D. Sideband Harmonic Suppression Analysis Based on Vector Diagrams for CHB Inverters Under Unbalanced Operation. *IEEE Trans. Ind. Electron.* **2023**, *71*, 427–437. [CrossRef]

24. Muhammad, T.; Khan, A.U.; Abid, Y.; Khan, M.H.; Ullah, N.; Blazek, V.; Prokop, L.; Misák, S. An Adaptive Hybrid Control of Reduced Switch Multilevel Grid Connected Inverter for Weak Grid Applications. *IEEE Access* **2023**, *11*, 28103–28118. [CrossRef]

25. Liu, H.-D.; Lin, C.-H.; Pai, K.-J.; Wang, C.-M. A GMPPT algorithm for preventing the LMPP problems based on trend line transformation technique. *Solar Energy* **2020**, *1*, 53–67. [CrossRef]

26. Zaky, A.A.; Elewa, S.; Alyahya, S.; Al-Dhaifallah, M.; Rezk, H.; Yousif, B. Mitigation of Temperature Effects and Performance Enhancement of Perovskite Solar Cells Using Nano-Pyramids Grating. *IEEE Access* **2023**, *11*, 36399–36408. [CrossRef]

27. Peng, Z.-W.; Buck, T.; Koduvelikulathu, L.J.; Mihailetchi, V.D.; Kopecek, R. Industrial Screen-Printed n-PERT-RJ Solar Cells: Efficiencies Beyond 22% and Open-Circuit Voltages Approaching 700 mV. *IEEE J. Photovolt.* **2019**, *9*, 1166–1174. [CrossRef]

28. Liu, H.; Nobre, A.M.; Yang, D.; Ye, J.Y.; Martins, F.R.; Rüther, R.; Reindl, T.; Aberle, A.G.; Peters, I.M. The Impact of Haze on Performance Ratio and Short-Circuit Current of PV Systems in Singapore. *IEEE J. Photovolt.* **2014**, *4*, 1585–1592. [CrossRef]

29. Choi, E.; Namgoong, G.; Park, W.; Kim, J.; Kim, S.; Lee, B.; Bien, F. A 1.4 mW to 119 mW, Wide Output Power Range Energy Harvesting System With 2-D Fast MPPT Based on HC for 1k to 50k Illuminated Solar Cell. *IEEE Trans. Circuits Syst. II Express Briefs* **2022**, *69*, 4389–4393. [CrossRef]

30. Ram, J.P.; Pillai, D.S.; Rajasekar, N.; Strachan, S.M. Detection and Identification of Global Maximum Power Point Operation in Solar PV Applications Using a Hybrid ELPSO-P&O Tracking Technique. *IEEE J. Emerg. Sel. Top. Power Electron.* **2022**, *8*, 1361–1374. [CrossRef]

31. Bahrami, M.; Zandi, M.; Gavagsaz, R.; Nahid-Mobarakeh, B.; Pierfederici, S. A new hybrid method of MPPT for photovoltaic systems based on FLC and three point-weight methods. In Proceedings of the 7th Power Electronics and Drive Systems Technologies Conference (PEDSTC), Tehran, Iran, 16–18 February 2016; pp. 446–450. [CrossRef]
32. Liu, H.-D.; Lin, C.-H.; Lu, S.-D.; Ahmad, J. A Novel VFVDC Optimized Full Bridge Inverter Control Strategy for Independent Solar Power Systems. *IEEE Access* **2022**, *10*, 2169–3536. [CrossRef]